Research Article

# Influence of three-dimensional transverse micro-ridges on the Poiseuille number in a gaseous slip flow

Richie Garg[1] · Amit Agrawal[1]

**Abstract**

Micro-ridges are regular micro-engineering structures protruding outward from the microchannel wall surface. The role of these micro-ridges in changing the friction factor ($f$) of a microchannel with internal rarefied gas flows is not explored in the literature. In this work, we present three-dimensional numerical simulations in a microchannel containing ridges arranged transverse to the flow direction. The length of the ridges is varied with respect to the pitch of the ridges; this ratio being christened as ridge fraction ($\delta$). The effect of $\delta$, ridge height ratio ($h/H$), Reynolds number ($Re$), Knudsen number ($Kn$) and Tangential momentum accommodation coefficient ($\alpha_v$) on the flow friction in terms of Poiseuille number ($fRe$) is investigated. In the continuum and slip regimes, it is found that $fRe$ decreases with an increase in $\delta$ and $h$ and a significant reduction in flow friction was shown with respect to a straight microchannel. There exists a critical height after which decrease in $fRe$ does not occur. Further, $fRe$ was observed to be a strong function of $Re$ at high $\delta$, which is attributed to the intensity of acceleration–deceleration experienced by the gas during the flow. Also, $fRe$ is established to be directly proportional to $\alpha_v$. The various flow characteristics are scrutinised where vortices are found trapped inside the ridge affecting the dynamics of flow in the ridges, whose size increases on increasing the gas rarefaction. This comprehensive investigation of behaviour of slip flow in complex microchannels will be useful in designing micro-devices with reduced friction.

**Keywords** Cavity · Surface texturing · Friction factor · Asymmetric vortex · Protrusions · Ridge critical height

## 1 Introduction

Micro-electro mechanical systems (MEMS) may have complex geometries superimposed with surface micro-structures in the form of textures and protruding ridges which can affect the flow locally in a non-trivial manner. The effect of ridges therefore cannot be neglected especially in rarefied gas flows. Most of the analytical, experimental and computational work deals with randomly distributed rough micro-structures, micro-cavities, textured, furrowed or wavy microchannels, but work on structured micro-ridges protruding outward from the channel wall surface is minimal [1]. In the current numerical investigation, it is found that the influence of ridges and rarefaction on Poiseuille number ($fRe$ where $f$ is friction factor and $Re$ is Reynolds number) on gas flow in microchannels is vigorously coupled.

There is a necessity of numerically studying the intricacies of ridge effects at micro-scale in slip flow regime. Mahulikar et al. [2] concluded that the effect of slip is to flatten the velocity distribution and reduce $f$ as compared to continuum flow. Compressibility leads to a non-linear axial pressure variation, while rarefaction decreases the curvature in pressure distribution. Therefore, the pressure distribution becomes linear again in the free-molecular flow regime [3]. Croce et al. [4] found that rarefaction has a significant impact on $fRe$, even at an exit $Kn$ as low as 0.0083. Numerical tool is preferred for such a study as

---

✉ Amit Agrawal, amit.agrawal@iitb.ac.in | [1]Department of Mechanical Engineering, Indian Institute of Technology Bombay, Powai, Mumbai 400076, India.

SN Applied Sciences (2019) 1:1035 | https://doi.org/10.1007/s42452-019-0991-5

Received: 20 May 2019 / Accepted: 26 July 2019 / Published online: 16 August 2019

the geometry of the flow passage and flow conditions are clearly known in this approach unlike in experiments. Two-dimensional (2D) approximation is insufficient to describe the real microchannel. The 2D approximation can enhance the strength of the vortices inside the ridges. In actual three-dimensional (3D) ridge elements, the flow may turn around the valley rather than filling it. Hence, 2D schematisation could be inappropriate for modelling the friction factor of a 3D microchannel. Our 3D simulations focus on external ridge elements aligned normal to the flow direction, to understand the friction resistance to the flow in such cases.

Since flow in microchannel can also be viewed as wavy channels, we briefly review the relevant literature based on numerical studies available for wavy and furrowed microchannels. Khan et al. [5] demonstrated better thermal–hydraulic performance for wavy as compared to straight channel based on printed circuit heat exchanger for three angles of zigzag bend with helium as the working fluid. Sarkar and Sharma [6] also found a monotonic increase in the ratio of $f$ and Nusselt number ($Nu = hD_h/k$, where $h$ is the convective heat transfer coefficient, $D_h$ is the hydraulic diameter and $k$ is the thermal conductivity of the flow medium), of a furrowed sinusoidal wavy channel with that of plane channel, with rising Re. The area goodness factor of a wavy channel as compared to a plane channel is found to decrease with increasing amplitude and remains almost constant with increasing wavelength of wavy channel. Harikrishnan and Tiwari [7] numerically studied effect of different skewness angles and wave amplitudes of a sinusoidal wavy channel. They found that both $Nu$ and $f$ increase up to a certain skewness angle, beyond which these parameters decrease.

Ridges are a form of micro-structures protruding outward from the channel wall surface, while cavities sink into the surface. A physical geographical analogy is that ridges are like hills on the Earth's surface and cavities are similar to valleys. Ridges and cavities appear together. In the present work, the height of a ridge is equal to the depth of a cavity. Ridges and cavities exist in applications like fuel cell devices, micro-heat sinks and exchangers, micro-mixers, pumps, turbines, valves and reactors. Cavities also appear at unwanted drag-increasing gaps between segments of aircraft skin, slots between moveable parts of control surfaces, ship hulls and slotted walls of transonic wind-tunnels [8]. Difficulties like store separation, optical distortion and structural damage can arise due to severe acoustic loading and self-sustained oscillations inside a cavity. According to Bres and Colonius [9], instabilities in the shear layer interact with the downstream corner in compressible flows. This creates acoustic waves propagating upstream and generating additional disturbances in the shear layer. This mechanism of cavity oscillations is called flow-acoustic resonance. Motivation for cavity research comes from noise reduction and substitution of active flow control devices with their passive counterparts. Bres and Colonius [9] carried out complete 3D global instability analysis over rectangular cavity for compressible flows. Shear-driven cavity incompressible flows have been investigated by Horner et al. [10], Vicente et al. [11], Romanò and Kuhlmann [12]. Vicente et al. [11] noted that spanwise dynamics occur in the recirculating flow in both shear and lid-driven cavities; this makes 3D flows significantly more complex than their 2D counterparts.

The numerical benchmark problem of lid-driven cavity has been a paradigm for solving vortex dynamics problems in closed systems [13]. Prior to this recent review on lid-driven cavity [13] is a two-decade old review by Shankar and Deshpande [14]. Mohammadzadeh et al. [15] studied circulation in lid-driven cavities and concluded that increment of non-equilibrium effects decreases the vortex strength as well as the propagation of downstream information. Reducing the wall velocity decreases the flow temperature and the induced shear forces by the driven lid to the flow. Naris and Valougeorgis [16] studied the rarefied gas flow in rectangular cavity driven by upper wall. They observed growing and collating of corner counter-rotating vortices on incrementing the cavity depth. Alkhalidi et al. [17] numerically investigated buoyancy driven rarefied gas inside a conjugate cavity of uniform wall temperature and found that the average $Nu$ is inversely proportional to $Kn$. Gat et al. [18] focussed on extending the analysis of Arkilic et al. [19] for compressible viscous flows to configurations with symmetric constriction or cavity. The present work also uses the analysis of Arkilic et al. [20] for the validation of our simulations. Yu et al. [21] used experimental and numerical techniques to study pressure driven gas and liquid flow in micro-cavities. According to them, the pressure gradient first decreases due to flow divergence into the cavity and then increases due to flow convergence into the main channel. The mass flow rate increases in multi-cavity channel due to reduction in drag locally along every cavity. This local cavity effect on pressure distribution could be detected only computationally because it is generally smaller than the experimental error. This establishes the necessity of numerical work to explore the local cavity and ridge effect.

Since pressure drop characteristics along the microchannels with ridges is crucial to arrive at an optimum structural size of a micro-device, the objectives of the current work are to (i) simulate flow over three-dimensional external ridge elements located on the side walls of a microchannel, (ii) investigate the effect of Reynolds number and ridge geometry on the frictional resistance in slip flow regime, (iii) explore the effect of rarefaction and TMAC on *fRe*, and (iv) uncover the flow physics inside the micro-ridge.

## 2 Methodology

Micro-ridge effect on *fRe* in the slip flow regime has been investigated using numerical simulations in this work (Fig. 1). The simulations are performed using Ansys Fluent 15.0. A pressure based solver with absolute velocity formulation and steady time is employed. Viscous laminar model with low pressure boundary slip (LPBS) option is applied.

Important parameters are defined in Eqs. 1, 2 and 3. Knudsen number ($Kn$) is the ratio of mean free path ($\lambda$) to the characteristic scale of gas flow, which is hydraulic diameter ($D_h = 4A_c/P$). Here, $A_c$ is area of cross-section and $P$ is perimeter. Note that $D_h$ is calculated on the basis of the main channel inlet cross-section and not the ridge cross-section.

$$Kn = \frac{\lambda}{D_h} = \frac{\mu}{PD_h}\sqrt{\frac{\pi RT}{2}} \tag{1}$$

$$Re = \frac{\dot{m}D_h}{\mu A_c} \tag{2}$$

$$fRe = 2\frac{\Delta P}{L}\frac{D_h^2 A_c \rho}{\dot{m}\mu} \tag{3}$$

where $\mu$ is viscosity of ideal gas, air ($\mu = 1.7894 \times 10^{-5}$ kg/m-s) taken at temperature ($T$) set as 300 K, $P$ is the pressure, $R$ is the specific gas constant, $Re$ is the Reynolds number, $\dot{m}$ is the specified mass flow rate, *fRe* is the Poiseuille number, $\Delta P$ is the pressure drop of the channel, and $\rho$ is density of ideal gas.

Five parameters, exit Knudsen number ($4.44 \times 10^{-4} < Kn < 2.07 \times 10^{-2}$), Reynolds number ($0.10 < Re < 50.31$), tangential momentum accommodation coefficient ($0.10 < \text{TMAC} < 0.926$), ridge fraction ($0 < \delta < 1$) and ridge height ratio ($0.05 < h/H < 1$) are varied to explore their influence on *fRe*. A large number of simulations (about 700) were therefore conducted as part of this study.

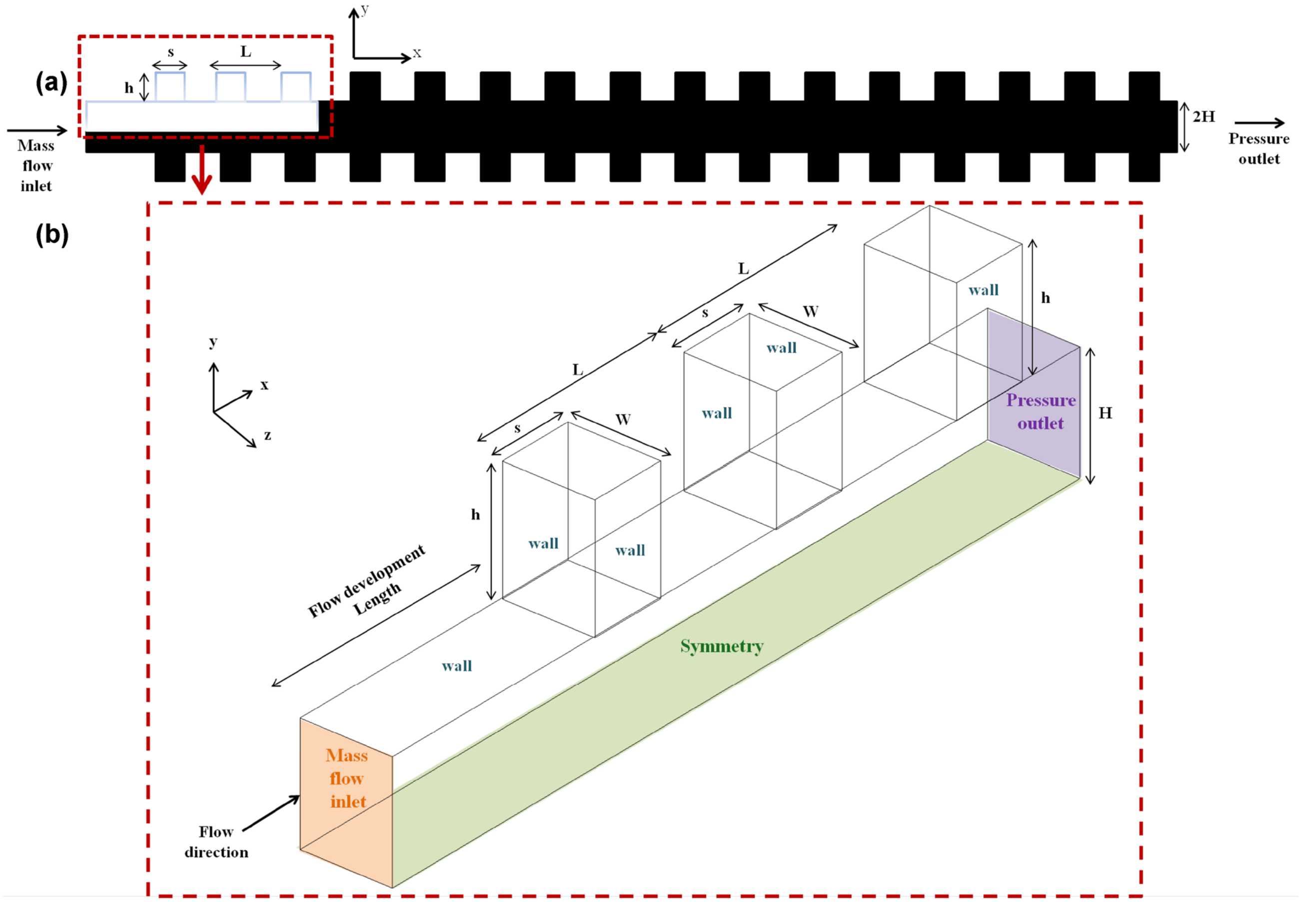

**Fig. 1** **a** Entire front view of 3-D microchannel with sixteen transverse ridges simulated with mass flow inlet and pressure outlet boundary conditions, **b** magnified view highlighting first three ridges

### 2.1 Governing equations

The governing equations include mass conservation,

$$\nabla.\left(\rho\vec{V}\right) = 0, \tag{4}$$

and momentum equations in $x$, $y$ and $z$ directions for compressible flow and energy equation are given by

$$\rho\left(\vec{V}.\nabla\right)u = -\frac{\partial p}{\partial x} + \mu\nabla^2 u + \frac{\mu}{3}\frac{\partial}{\partial x}\left(\nabla.\vec{V}\right), \tag{5}$$

$$\rho\left(\vec{V}.\nabla\right)v = -\frac{\partial p}{\partial y} + \mu\nabla^2 v + \frac{\mu}{3}\frac{\partial}{\partial y}\left(\nabla.\vec{V}\right), \tag{6}$$

$$\rho\left(\vec{V}.\nabla\right)w = -\frac{\partial p}{\partial z} + \mu\nabla^2 w + \frac{\mu}{3}\frac{\partial}{\partial z}\left(\nabla.\vec{V}\right), \tag{7}$$

$$\nabla.\left(\vec{V}(\rho E + p)\right) = \nabla.(k\nabla T) \tag{8}$$

We have used the default Maxwell's model (Fluent Inc. Theory guide, 2010). Slip velocity is given by Eq. 9 and temperature jump is given by Eq. 10.

$$u_w - u_g = \left(\frac{2-\alpha_v}{\alpha_v}\right)Kn\frac{\partial u}{\partial n} \tag{9}$$

$$T_w - T_g = 2\left(\frac{2-\alpha_T}{\alpha_T}\right)Kn\frac{\partial T}{\partial n} \tag{10}$$

where $\vec{V}$ is the velocity vector with $u$, $v$ and $w$ being the velocity components in streamwise, cross-streamwise and spanwise directions. The subscripts $g$ and $w$ represent gas and wall respectively. $n$ is the normal to the wall. $\alpha_v$ is TMAC of the gas taken as 0.1, 0.3, 0.5, 0.7 and 0.926. The last value is suggested by Agrawal and Prabhu [22] based on a detailed survey of experimental data. $T$ is the temperature, $\rho$ is density, $E$ is energy ($E = h - p/\rho + V^2/2$), $h$ is sensible enthalpy, $p$ is pressure, $k$ is thermal conductivity of fluid, and $\alpha_T$ is the thermal accommodation coefficient with a value of 0.9137. Viscous dissipation term is included in the energy equation for the highest and lowest values of TMAC, Mach number, Knudsen number, Reynolds number of all ridge fractions, and Poiseuille number (*fRe*) is compared to that without inclusion of viscous dissipation. The per cent deviation in *fRe* is found to be less than 1%. Therefore, viscous heating is negligible in our work.

### 2.2 Geometry and boundary conditions

Figure 1a depicts the front view of three dimensional microchannel with transverse ridges, where first three ridges are highlighted. A zoomed view with all the prescribed boundary conditions is illustrated schematically in Fig. 1b. Microchannel is simulated with mass flow inlet and pressure outlet boundary conditions. Since, the flow is compressible, a flow development length of 800 µm is provided, which is double of that required at the maximum value of *Re* considered in this study.

A parameter, ridge fraction ($\delta$) is defined as the ratio of length ($s$) of a protruded ridge to the pitch of the ridges ($L$) (Fig. 1b). For fixed $L = 200$ µm, $s$ is varied as 0, 50, 100 and 150 µm. Therefore, $\delta$ values of 0, 0.25, 0.5 and 0.75 are obtained. $\delta = 0$ corresponds to smooth microchannel without ridges. These are simulated to compare the ridge effect on *fRe* with baseline case of smaller straight channel. Sixteen ridges of each ridge fraction for a given length are modelled. The height ($2H$, due to symmetry) of channel is 200 µm and width ($W$) is 100 µm, making the aspect ratio ($\alpha = W/2H$) of the channel as 0.5. The width of the protruded ridge is same as the width of the main channel ($W$) as shown in Fig. 1b. The height ($h$) of the ridge is varied as 100, 50, 40, 30, 20, 10 and 5 µm. Height of the ridge is nondimensionalised by half the height of the channel ($h/H$).

Air is assumed to behave as an ideal gas. At the bottom surface, symmetry boundary condition [4, 23] is applied. Mass flow inlet boundary condition is applied at the inlet of the microchannel with mass flow rate varying from $1.35 \times 10^{-10}$ to $2.25 \times 10^{-7}$ kg/s. At the exit of microchannel, pressure outlet boundary condition is allocated in order to fix Knudsen number from $4.44 \times 10^{-4}$ to $2.07 \times 10^{-2}$.

The SIMPLE scheme is employed with least square cell based spatial discretisation and second order upwind for better accuracy. The convergence of continuity, momentum and energy equations is checked with residuals of the order of $10^{-9}$. Pressure drop calculations are performed for each $\delta$, *Re*, *Kn* and TMAC case and converted into Poiseuille number (*fRe*) as given by Eq. 3 [4, 23, 24].

### 2.3 Grid independence test

Maximum Knudsen number ($Kn = 2.07 \times 10^{-2}$), Reynolds number ($Re = 50.31$) and ridge fraction ($\delta = 0.75$) cases are chosen for performing grid independence test for four ridges. This case is chosen since it has the maximum influence on *fRe*, as indicated in Fig. 6e (presented later). In Table 1 (in bold), it is observed that a hexahedral mesh size of 4 µm gives a deviation of 0.76% as compared to a mesh size of 2 µm. Even 5 µm mesh size gives a deviation within 1%. Hence, 4 µm size is selected for all the simulations with ridge height of 20 µm and above to save computational time and power (Fig. 4a; presented later). For shorter ridge heights of 0.5, 5 and 10 µm, the grid is drastically refined up to 0.05 µm in the cross-streamwise direction leading

**Table 1** Grid independence test

| Mesh size (μm) | No. of mesh volumes | *ΔP/L* (Pa/m) | *fRe* | Per cent deviation w.r.t 2 μm |
|---|---|---|---|---|
| 2 | 2,760,000 | 1,099,580.00 | 54.06 | – |
| 3 | 799,326 | 1,094,788.75 | 53.82 | 0.43 |
| **4** | 346,875 | 1,091,282.50 | 53.65 | **0.76** |
| 5 | 176,000 | 1,089,736.25 | 53.57 | 0.90 |
| 6 | 106,063 | 1,084,712.50 | 53.33 | 1.37 |
| 7 | 61,544 | 1,071,066.25 | 52.65 | 2.66 |

The value in bold indicates the grid size selected for the present study

to mesh volumes up to 1,313,500 to ensure the solution is grid independent.

### 2.4 Validation of results with analytical solution and DSMC data

The validation of simulations performed by benchmarking against two-dimensional channel solution for compressible flow is presented in this section. A parallel plate microchannel of height 1 μm and length 10 μm is taken. The centre-line pressure distribution is compared with the analytical solution of non-linear pressure distribution reported by Arkilic et al. [20]. The present predictions are also compared with the DSMC data of compressible flow provided by Gavasane et al. [25] on Argon gas for $Kn = 0.124$ at channel outlet, as illustrated in Fig. 2a. The mass flow rate specified at inlet of this geometry has been computed from the solved DSMC data. The results obtained for the absolute pressure are in good agreement with the analytical solution as well as the DSMC data. The centre-line velocity distribution obtained by the present simulation matches well with that of DSMC data (Fig. 2b). Centre-line static temperature distribution (Fig. 2c) obtained in streamwise direction matches with DSMC data, hence the energy equation is validated. Any minor difference in comparison is due to use of pressure inlet boundary condition in DSMC and mass flow inlet boundary condition in Fluent. This difference is insignificant to comprehend the flow physics further away from channel boundaries. Similarly, the slip velocity in streamwise direction plotted at cell adjacent to the wall is in good agreement with DSMC (Fig. 2d). The cross-streamwise velocity distribution plotted at half of the channel length ($x/L = 0.5$) is in excellent agreement with that of DSMC data (Fig. 2e) as well as analytical solution for first and second-order slip boundary conditions given by Karniadakis et al. [26]. Hence, the boundary conditions used are validated.

The incompressible flow results for three-dimensional straight channel of with aspect ratio, $\alpha = 0.5$ are compared with analytical solution reported by Morini et al. [27] (Eq. 11).

$$fRe = \frac{62.192}{1 + 8.571Kn} \tag{11}$$

Poiseuille number (*fRe*) of straight channel reported by them is 61.956, and that obtained in this work is 61.698 which give a percentage difference of 0.4%. There is an excellent agreement with the corresponding analytical solution at all *Re* in the continuum regime, where $Kn = 4.44 \times 10^{-4}$. Validation in the slip regime has been performed at four different Knudsen numbers (Table 2). At highest $Kn = 2.07 \times 10^{-2}$, deviation of *fRe* from analytical solution is minimum (in bold), trusting us with working in the rarefied gas flow regime. Since, *fRe* of straight channel is matching very well with the analytical solution [27]; this gives us the confidence to introduce the ridges in the straight channel.

## 3 Results and discussion

The hydraulic diameter ($D_h$) is 133.33 μm for all the ridge fractions. *Kn* at the outlet of channel and *Re* are calculated based on $D_h$ according to Eqs. 1 and 2 respectively. The mass flow rate is specified from $1.35 \times 10^{-10}$ kg/s ($Re = 0.10$), $1.35 \times 10^{-8}$ kg/s ($Re = 10.06$), $3.375 \times 10^{-8}$ kg/s ($Re = 25.15$), $5.40 \times 10^{-10}$ kg/s ($Re = 40.24$) and $6.75 \times 10^{-8}$ kg/s ($Re = 50.31$). The exit *Kn* and *Re* are kept same for all *δ*. Table 3 gives the combination of all the specific parameters used for about 700 three-dimensional simulations conducted. The flow characteristics inside ridges with mass flow inlet and pressure outlet boundary conditions are depicted for the highest exit Knudsen number of this study, $Kn = 2.07 \times 10^{-2}$. In the later subsections, the combined effect of *Re*, *δ* and *Kn* on *fRe* is extensively explained.

### 3.1 Effect of Reynolds number on the flow characteristics inside a ridge

The flow characteristics inside ridges of $\delta = 0.75$ are depicted by streamtraces, absolute pressure, *x*-velocity, *y*-velocity and vorticity at $Kn = 2.07 \times 10^{-2}$ (Fig. 3). These contours are compared at minimum and maximum Reynolds numbers ($Re = 0.10$ and 50.31) to investigate the influence of *Re*. All the contours are drawn at the mid-plane along *z*–direction, which is located at $z/H = 0.5$ for $\delta = 0.75$. This ridge fraction is chosen because it gives the lowest *fRe* value of 44.02 in the investigated range of *Kn*, *Re* and *δ*, as described in subsequent Sect. 3.2. The velocity profiles are qualitatively similar at the entrance of each ridge, once the

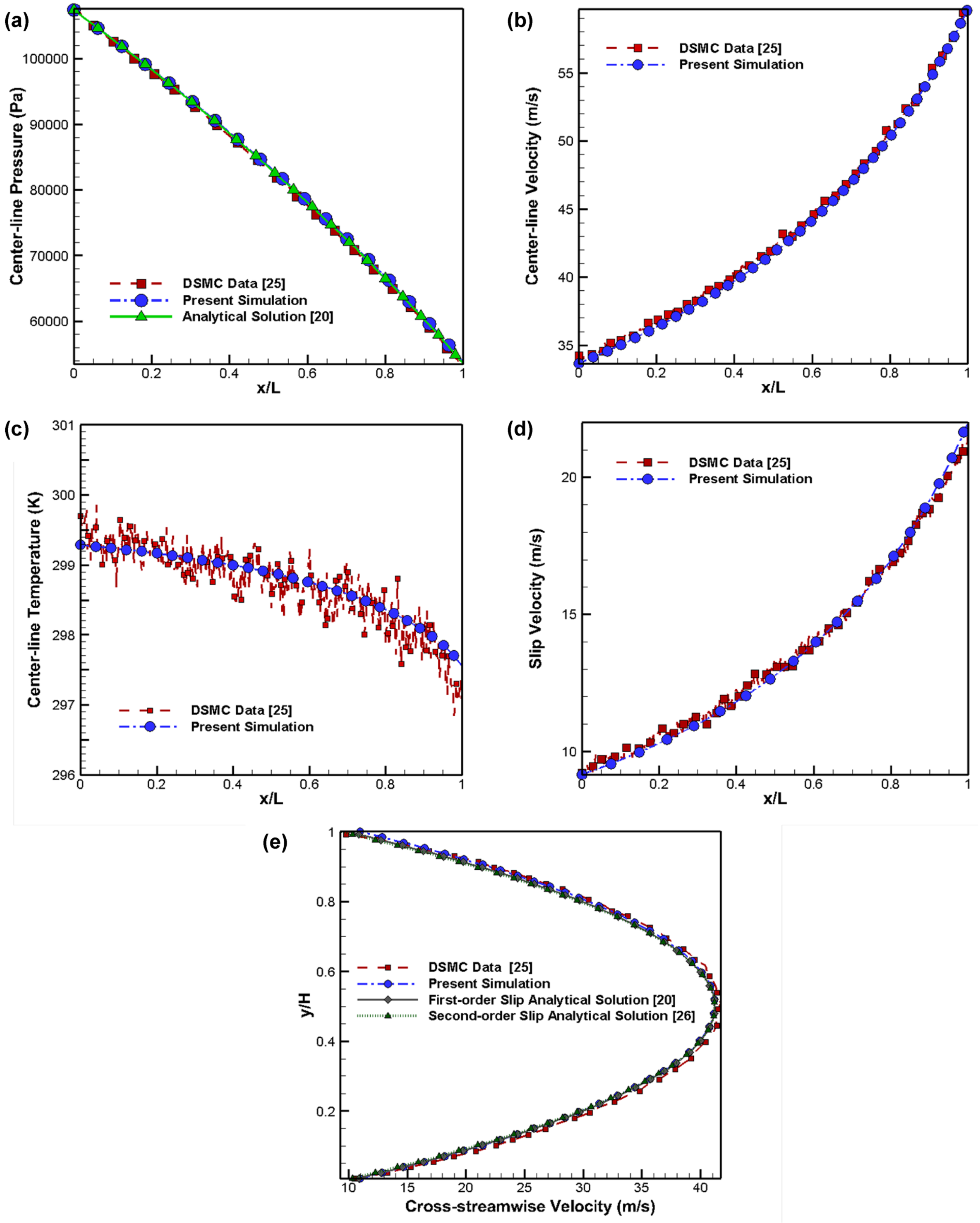
(a)
Center-line Pressure (Pa)
100000
90000
80000
70000
60000
x/L
0
0.2
0.4
0.6
0.8
1
DSMC Data [25]
Present Simulation
Analytical Solution [20]
(b)
Center-line Velocity (m/s)
55
50
45
40
35
x/L
DSMC Data [25]
Present Simulation
(c)
Center-line Temperature (K)
301
300
299
298
297
296
x/L
DSMC Data [25]
Present Simulation
(d)
Slip Velocity (m/s)
20
15
10
x/L
DSMC Data [25]
Present Simulation
(e)
y/H
1
0.8
0.6
0.4
0.2
Cross-streamwise Velocity (m/s)
10
15
20
25
30
35
40
DSMC Data [25]
Present Simulation
First-order Slip Analytical Solution [20]
Second-order Slip Analytical Solution [26]

◂**Fig. 2** A comparison between variations of **a** centre-line pressure distribution along streamwise direction obtained in present simulation with analytical solution of Arkilic et al. [20] and DSMC data of Gavasane et al. [25], **b** centre-line velocities along streamwise direction, **c** centre-line static temperature distribution along streamwise direction, **d** slip velocity adjacent to the wall along streamwise direction, **e** cross-streamwise velocity profile obtained at half length of the channel, obtained in simulation, DSMC data [25], analytical solution of Karniadakis et al. [26] for first and second-order slip boundary conditions

gas passes through the flow development length. The flow characteristics depicted for sixteen ridges are zoomed in the 8th, 9th, 10th and 11th ridges for clarity. The dimensions of the channel in x, y and z coordinates are non-dimensionalised by hydraulic diameter. Overall, it can be observed that flow is behaving in a periodic manner. The same flow pattern is repeating after every ridge, indicating that the periodicity is same as the pitch length.

Figure 3a, b shows the comparison of streamtraces in all sixteen ridges at $Re = 0.10$ and 50.31. Figure 3c, d depicts the magnified view of streamtraces of 8th, 9th, 10th and 11th ridges. Upon examining the pattern in Fig. 3c, the streamlines move very smoothly inside the ridges at low $Re = 0.10$, whereas Fig. 3d depicts the presence of trapped vortices at $Re = 50.31$. This indicates that there is an exchange of momentum from the main channel to the ridge, which is more pronounced for $Re = 50.31$. A counter-clockwise vortex is trapped in every ridge. This phenomenon of creation of eddies is also observed by Naris and Valougeorgis [16].

The absolute pressure in Fig. 3e, *f* is non-dimensionalised by pressure at the outlet of the channel. At $Re = 0.10$, low pressure is seen at ridges due to extremely low flow rate of $1.35 \times 10^{-10}$ kg/s. At $Re = 50.31$, the magnitude of lowest pressure is more than the highest pressure at $Re = 0.10$. Overall, the range of absolute pressures and pressure drop in ridges is higher at $Re = 50.31$ compared to that at $Re = 0.10$.

Figure 3g shows the streamwise velocity distribution at $Re = 0.10$. All the velocities are normalised with respect to the average velocity at the inlet of the main channel. At $y = 0$, there is higher *x*-velocity, which gradually reduces as the flow approaches the mouth of the ridge (located at $y = H$), and further reduces till the topmost wall of the ridge. As the streamlines enter the ridge mouth, the area for the flow increases which leads to a reduction in velocity according to mass conservation. The magnitudes of *x*-velocity are higher at $Re = 50.31$ (Fig. 3h) as opposed to those at $Re = 0.10$. As apparent from the velocity contours, the flow is not symmetric along the vertical centre-line of the ridge. The velocity peaks rather drift slightly towards the right side of the centre-line. However, notice from Fig. 3g that the flow is symmetric along vertical centre-line at $Re = 0.10$. This indicates that there is a phenomenon happening inside the ridge, which is leading to this drift of velocity peaks, upon increasing the Reynolds number. This observation becomes clear upon examining the streamline pattern in Fig. 3b, d which depicts the presence of trapped vortices. At $Re = 50.31$, due to the presence of vortex, all the velocity peaks are drifted slightly away from the vertical centre-line of the ridge and the flow becomes non-symmetric, unlike symmetric flow observed at $Re = 0.01$. Moreover, the vortex is itself not symmetric, as it is clinging towards the left corner. This could be because of the flow entering the ridge at an angle from the left corner. While exiting from the ridge, flow hits the right corner, thus vortex gets drifted away from the right corner.

Figure 3i, j depicts a comparison of the cross-streamwise velocities. At $Re = 0.10$ and $Re = 50.31$, a high positive magnitude of *y*-velocity is observed at the left corner of the ridge and high negative magnitude is seen at the right corner of the ridge, because of the flow impacting the wall before exiting the right corner of the ridge. In between these two corners, the *y*-velocity variation from positive to negative is more gradual at $Re = 50.31$ (Fig. 3j) compared to that at $Re = 0.10$ (Fig. 3i).

Figure 3k, l shows vorticity contours orthogonal to streamwise and cross-streamwise directions. The vorticity is multiplied by $D_h$ and divided by inlet velocity to make it non-dimensional. The *z*-vorticity magnitude is higher in the corners of the ridge compared to other regions. At $Re = 0.10$, *z*-vorticity is symmetric along the vertical centre-line of the ridge, but not at $Re = 50.31$. Similar phenomenon is reported for incompressible flow in lid-driven cavity flow by Kuhlmann and Romanò [13] as well as in shear-driven cavity flow by Romanò and Kuhlmann [12]. At $Re = 1$, streamlines are almost symmetrical due to symmetries of Navier–Stokes equation in Stokes flow limit of *Re* tending to zero. At greater *Re*, inertia terms in incompressible Navier–Stokes equations deteriorate the reflectional symmetry in the flow direction [13]. Horner et al. [10] also observed asymmetry in manifold structure of shear-driven cavity for incompressible flows due to inertia. Moreover, at $Re = 50.31$, the *z*-vorticity is lower at right corner as compared to that at left corner (Fig. 3l). This is because of flow hitting the right corner before exiting the ridge. This creates higher pressure and lower velocity gradients at right corner, leading to lower vorticity.

Figure 4a shows the 3D view of two locations, $s_0$ which is the entrance of ridge expansion region and $s_{1/2}$ which is the ridge vertical centre-line. Figure 4b represents 2D view of $s_0$ and $s_{1/2}$ where normalised cross- streamwise velocity variation is plotted for $Re = 0.10$ and $Re = 50.31$. The velocity is normalised with the average velocity at the inlet of the straight channel ($\delta = 0$) after a flow development length of 800 μm (Fig. 4a). One of the middle

**Table 2** Validation of *fRe* for straight microchannel ($\alpha = 0.5$) with analytical solution of Morini et al. [27]

| Exit *Kn* (x/L = 1) | Mean *Kn* (x/L = 0.5) | *fRe* (present simulation) | *fRe* (Morini et al. [27]) | Per cent deviation |
|---|---|---|---|---|
| $4.44 \times 10^{-4}$ | $3.70 \times 10^{-4}$ | 61.698 | 61.956 | 0.416 |
| $4.61 \times 10^{-3}$ | $3.67 \times 10^{-3}$ | 59.423 | 59.931 | 0.846 |
| $1.01 \times 10^{-2}$ | $7.07 \times 10^{-3}$ | 57.481 | 57.977 | 0.854 |
| $1.50 \times 10^{-2}$ | $9.19 \times 10^{-3}$ | 56.461 | 56.823 | 0.637 |
| $\mathbf{2.07 \times 10^{-2}}$ | $1.09 \times 10^{-2}$ | 55.754 | 55.932 | **0.318** |

The value in bold indicates the *Kn* value where minimum deviation is obtained with respect to the analytical solution

**Table 3** Specific values of parameters simulated

| Ridge fraction ($\delta$) | Height ratio (*h/H*) | TMAC ($\alpha_v$) | Reynolds number (*Re*) | Exit Knudsen number (*Kn*) |
|---|---|---|---|---|
| 0, 0.25, 0.5, 0.75 | 0.05, 0.1, 0.2, 0.3, 0.4, 0.5, 1 | 0.1, 0.3, 0.5, 0.7, 0.926 | 0.101, 10.061, 25.154, 40.246, 50.307 | $4.44 \times 10^{-4}$, $4.61 \times 10^{-3}$, $1.01 \times 10^{-2}$, $1.50 \times 10^{-2}$, $2.07 \times 10^{-2}$ |

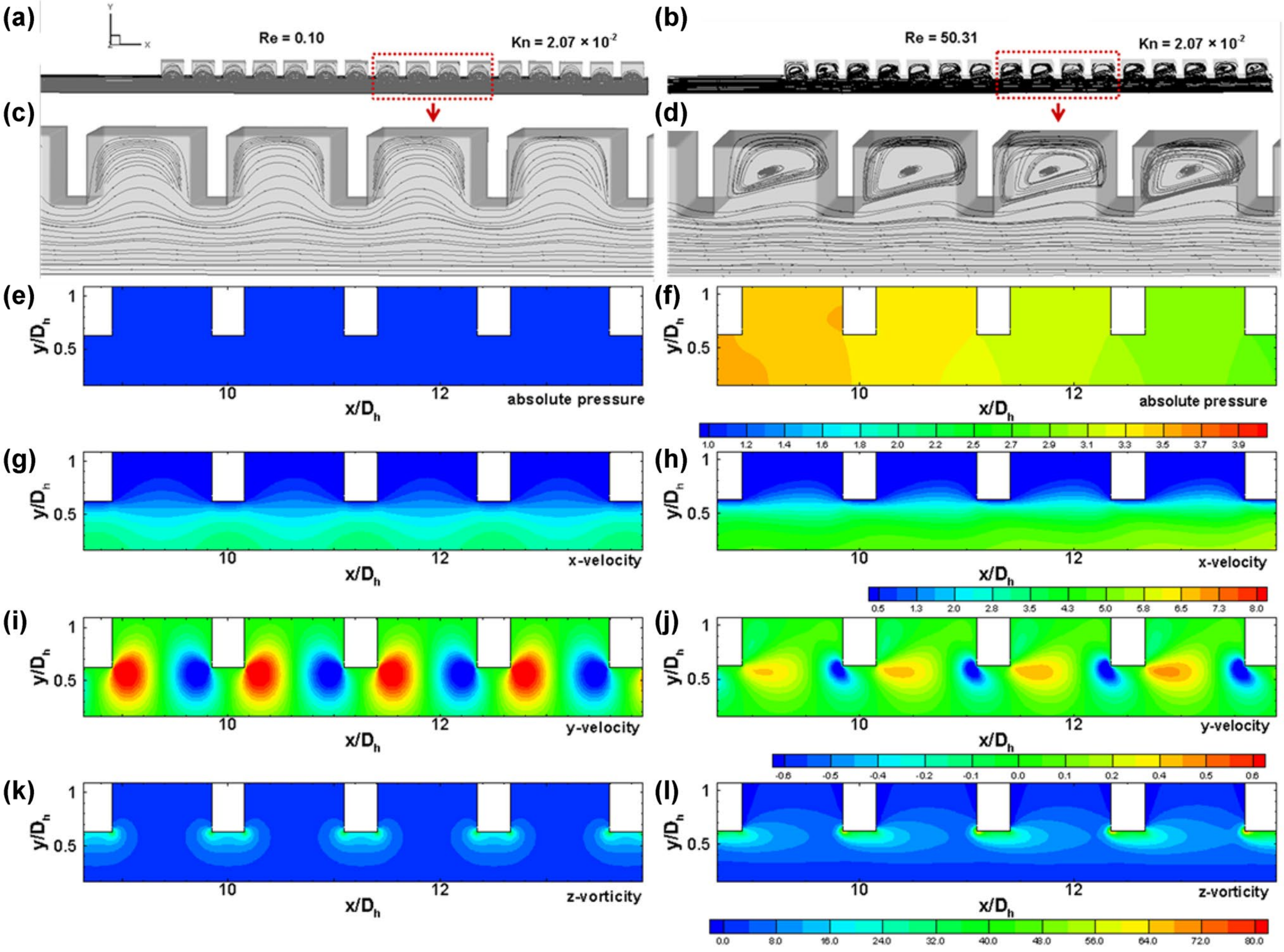

**Fig. 3** Comparison of flow characteristics of $\delta = 0.75$ for minimum and maximum *Re*, at exit $Kn = 2.07 \times 10^{-2}$; left column $Re = 0.1$, right column $Re = 50.31$. **a**, **b** Streamtraces for 16 ridges; **c**, **d** streamtraces in magnified view of 8th, 9th, 10th and 11th ridges; **e**, **f** absolute pressure variation; **g**, **h** streamwise velocity variation; **i**, **j** cross-streamwise velocity variation; **k**, **l** vorticity variation

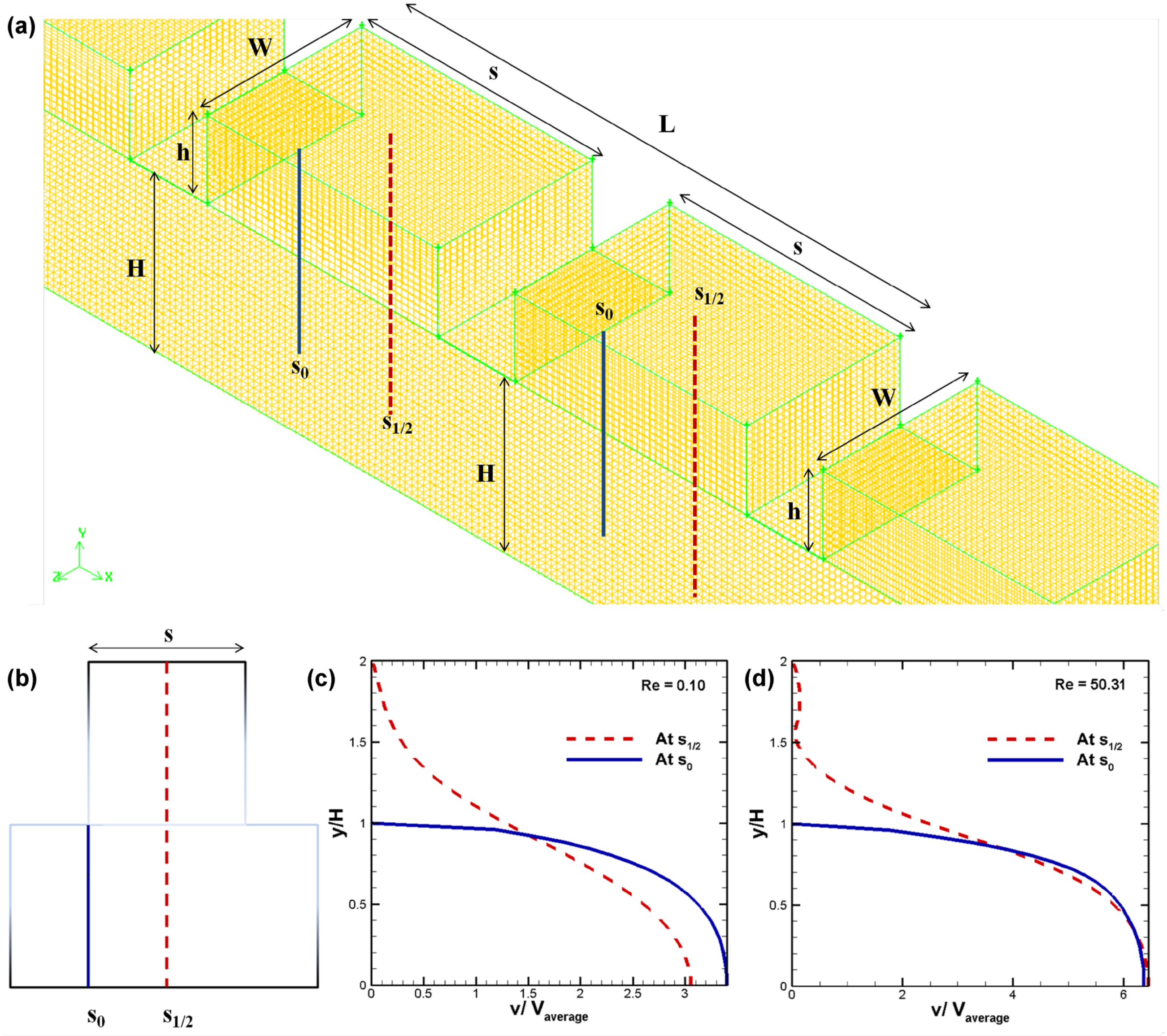

**Fig. 4** **a** Three-dimensional representation of hexahedral mesh of size 4 µm representing two locations, entrance of ridge expansion ($s_0$) and ridge vertical centre-line ($s_{1/2}$), **b** two-dimensional representation of $s_0$ and $s_{1/2}$, where comparison of cross-streamwise velocity profiles obtained for $Kn = 2.07 \times 10^{-2}$ at **c** $Re = 0.10$ and **d** $Re = 50.31$

ridges (thirteenth) is chosen for plotting the velocity variation to avoid any effect of boundary conditions. In Fig. 4b, c, the two curves meet at a point where the velocity at $s_{1/2}$ becomes equal to velocity at $s_0$. This point is christened as 'intersection point' which is the point where the velocities are equal for the flow just entering the ridge expansion region and ridge vertical centre-line. This helps in identifying the position at which momentum exchange is expected. Intersection point is located below the ridge mouth ($y = H$). Hence, there is an exchange of momentum from the main channel to the ridge at intersection point below the ridge mouth. This momentum exchange is more rapid for $Re = 50.31$, since the two curves intersect much earlier, at about $y/H = 0.25$ and again at about $y/H = 0.8$ (Fig. 4d).

Figure 5a depicts a comparison of the normalised streamwise velocities in the slip and continuum regimes at $Re = 0.10$, obtained at the mouth of the ridge ($y = H$). The velocities are normalised with respect to the average velocity at the inlet of the straight channel after flow development length (Fig. 1b). There is a strong effect of slip seen at $Kn = 2.07 \times 10^{-2}$. The magnitude of streamwise velocity at $Kn = 2.07 \times 10^{-2}$ is lower than that at $Kn = 4.44 \times 10^{-4}$ at $Re = 0.10$. A curious dip is seen at the velocity profile near the top wall of the ridge, which is explained by the streamline pattern in Fig. 3a. As the streamlines enter the

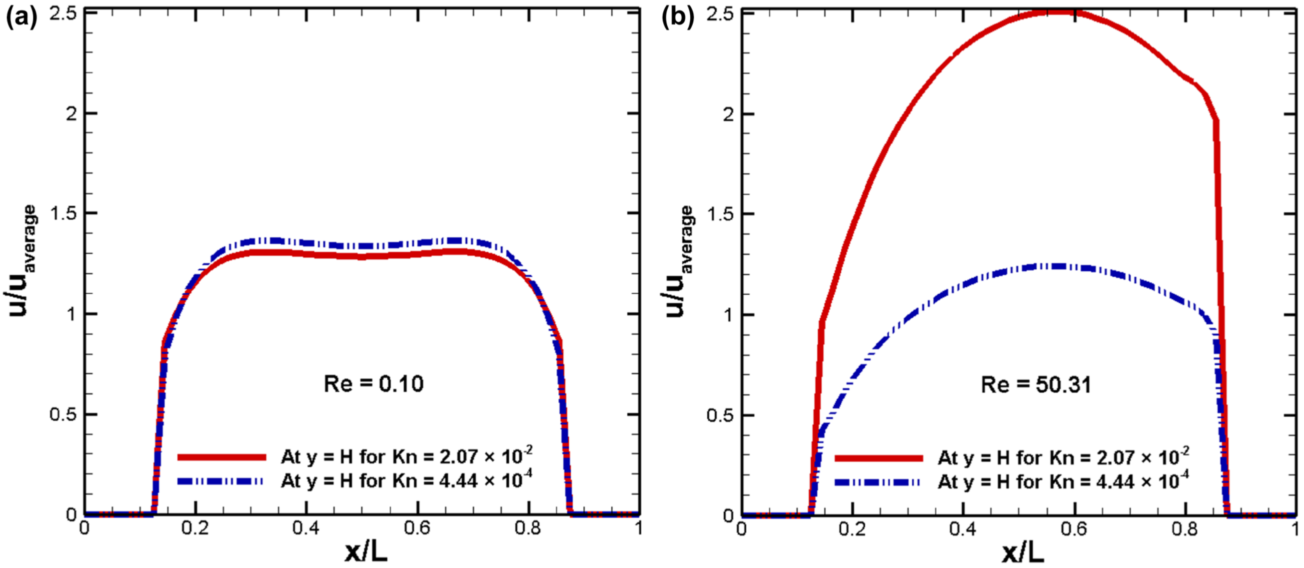

**Fig. 5** Comparison of velocity profile obtained at the mouth of the ridge (located at $y=H$) in slip and continuum regime at **a** $Re=0.10$ and **b** $Re=50.31$

ridge mouth, the area for the flow increases which leads to a reduction in velocity according to mass conservation. However, at $Re=50.31$, the velocity magnitude at $Kn=2.07\times10^{-2}$ is comparatively much greater than that at $Kn=4.44\times10^{-4}$ (Fig. 5b).

This section helped in comparing of flow characteristics inside a micro-ridge for low and high *Re* at a specific *Kn*. The key point is the formation of vortices at $Re=50.31$ for $Kn=2.07\times10^{-2}$, which are absent at $Re=0.10$. This understanding of the influence of *Re* on micro-ridge flow physics provides a vivid picture for further understanding of *Re* influence on *fRe*, which is another key objective of this work. Since, this section focussed on flow characteristics of only a specific *Kn* and *δ* value, later sections explain *Re* influence on *fRe* over wide ranges on *Kn* and *δ*.

### 3.2 Effect of Reynolds number and ridge fraction on Poiseuille number

In this subsection, *fRe* for a wide range of *Re* is plotted for the ridges in Fig. 6a–c for exit $Kn=4.44\times10^{-4}$, $4.61\times10^{-3}$ and $2.07\times10^{-2}$, respectively. As explained in Sect. 2.4, *fRe* results for straight microchannel of aspect ratio, $\alpha=0.5$ are validated with *fRe* value reported by Morini et al. [27].

In the continuum regime (Fig. 6a), the value of *fRe* is nearly constant for $\delta=0.25$, whereas *fRe* increases slightly with *Re* for *δ* values 0.50 and 0.75. The increase is more prominent for higher *δ*. It is interesting to note that none of the four graphs intersect each other. In case of $\delta=0.75$, even after exhibiting a noteworthy climb of *fRe* with increase in *Re*, the plot does not touch the other plots in the investigated range. At lowest $Re=0.10$, *fRe* of $\delta=0.75$ is 15.5% less than *fRe* of $\delta=0$ while *fRe* of $\delta=0.50$ is 6.8% less than that of $\delta=0$. Therefore, at low *Re*, *fRe* is quite low, indicating less distortion of streamlines and penetrability into the ridges due to expansion and contraction cycles. As *Re* increases, streamlines distort and gas penetrates more, leading to a higher frictional resistance.

At exit $Kn=4.61\times10^{-3}$, $1.01\times10^{-2}$, $1.50\times10^{-2}$ and $2.07\times10^{-2}$ (Fig. 6b, c), *fRe* value at low *Re* has reduced for all microchannels with ridges, as compared to continuum regime, indicating that *fRe* decreases with *Kn*. At $Kn=4.61\times10^{-3}$, $\delta=0.50$ and lowest $Re=0.10$, *fRe* has decreased by 6.68% with respect to $\delta=0$ while at highest $Re=50.31$, *fRe* has decreased by 5.70%. For $\delta=0.75$, at $Re=0.10$, *fRe* has decreased to 15.22% with respect to $\delta=0$ and decreased to 11.99% at $Re=50.31$. At higher *Kn* values, *fRe* increases with *Re*. The reason for increase in *fRe* with *Re* is due to formation of vortices inside the ridges and distortion of streamlines, as shown in Fig. 3d. At $Kn=1.01\times10^{-2}$ and $Re=0.10$, *fRe* has decreased by 6.40% for $\delta=0.50$ and 14.83% for $\delta=0.75$, whereas at $Re=50.31$, has decreased by 5.82% for $\delta=0.50$ and 12.21% for $\delta=0.75$ with respect to $\delta=0$ (Fig. 6c). Similarly at $Kn=1.50\times10^{-2}$, *fRe* has decreased by 6.13% for $\delta=0.50$ and 14.45% for $\delta=0.75$ at $Re=0.10$, whereas at $Re=50.31$, has decreased by 5.83% for $\delta=0.50$ and 12.17% for $\delta=0.75$ with respect to $\delta=0$ (Fig. 6d).

At $Kn=2.07\times10^{-2}$ (Fig. 6e), for $\delta=0.50$, at lowest $Re=0.10$, *fRe* has decreased by 5.80% compared to that of $\delta=0$ while at $Re=50.31$, *fRe* has similarly decreased by 5.79%. For $\delta=0.75$, at $Re=0.10$, *fRe* has decreased

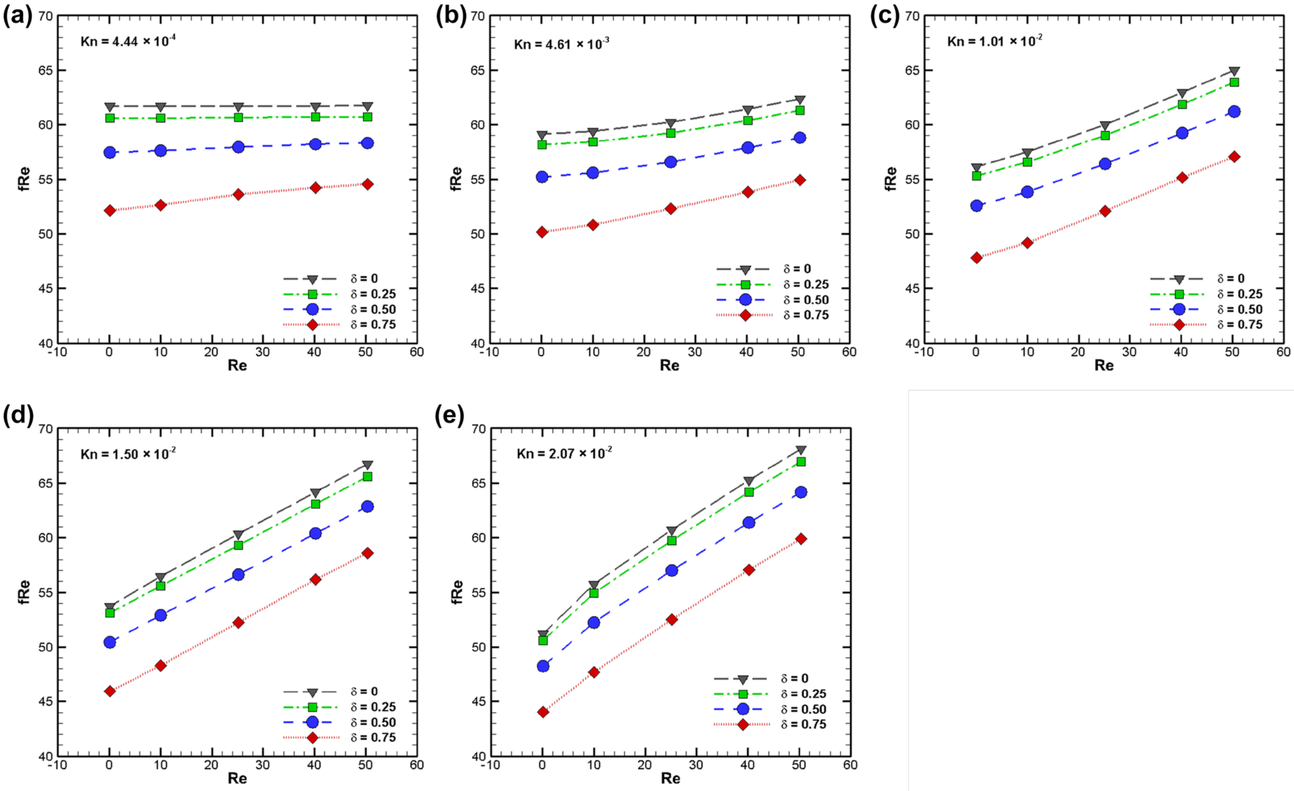

**Fig. 6** Effect of Reynolds number on Poiseuille number at all ridge fractions, compared to straight channel at exit Knudsen number **a** $4.44\times10^{-4}$, **b** $4.61\times10^{-3}$, **c** $1.01\times10^{-2}$, **d** $1.50\times10^{-2}$ and **e** $2.07\times10^{-2}$

by 14.01% compared to that of $\delta=0$ and decreased by 12.01% at $Re=50.31$. Dorari et al. [23] found recirculation zones due to pressure vibration, which are considered as dead zones with slip velocities almost zero, hindering the upstream gas flow and causing increase in flow resistance.

### 3.3 Effect of rarefaction on Poiseuille number

In Fig. 5 of Sect. 3.1, rarefaction highly influenced the streamwise velocity profile obtained at the ridge mouth. Thus arises the need for focussing upon the effect of *Kn* on *fRe*. Figure 7 shows the trend of *fRe* with *Kn* at five different Reynolds numbers. The present straight channel plot for $\delta=0$ and $\delta=0.25$ are quite close to each other for all *Re* values. In Fig. 7a, b, *fRe* for $\delta=0.5$ and 0.75 is less compared to *fRe* for $\delta=0.25$ and reduces further as *Kn* increases for $Re=0.10$ and 10.03. The behaviour of inverse proportionality of *fRe* with *Kn* is also reported by Morini et al. [27]. In Fig. 7c at $Re=25.15$, *fRe* reduces up to $Kn=4.61\times10^{-3}$ and becomes nearly constant with increasing *Kn* for all ridge fractions. In Fig. 7d at $Re=40.24$, *fRe* reduces up to $Kn=4.61\times10^{-3}$ and starts increasing with *Kn* for all ridge fractions. Hence, rarefaction beyond threshold $Kn=4.61\times10^{-3}$, there is a direct proportionality of *fRe* with *Kn* observed after a threshold $Re=25.15$.

Figure 7e shows the trend of *fRe* with *Kn* at highest $Re=50.31$. As *Kn* increases, *fRe* increases. This reflects the strong effect of *Re* on *fRe*. The present work elaborates about decrease in *fRe* of $\delta=0.5$ and 0.75 compared to straight channel ($\delta=0$), on increasing $\delta$ is much stronger on gas flow with lower *Kn*. For instance, at $Re=0.1$, $\delta=0.5$, the decrease is 6.68% at $Kn=4.61\times10^{-3}$ and 5.8% at $Kn=2.07\times10^{-2}$ as seen in Fig. 6a. Similarly at $Re=0.1$, $\delta=0.75$, the decrease is 15.22% at $Kn=4.61\times10^{-3}$, whereas 14.1% for $Kn=2.07\times10^{-2}$ (Fig. 6c). Therefore, the ridge elements assist the upstream gas flow and decrease *fRe* due to increment in flow area.

Figure 8 compares the streamtraces of ridges of $\delta=0.75$ at minimum and maximum exit *Kn* and same $Re=50.31$. As observed in Fig. 8, the size of vortex is smaller at $Kn=4.61\times10^{-3}$ as compared to that at $Kn=2.07\times10^{-2}$. On the increment of vortex size at higher *Kn*, flow area is expected to reduce due to which *fRe* is more compared to lower *Kn* (Fig. 7d–e). This might be the reason for the increasing trend of *fRe* with *Kn* noticed at high *Re*.

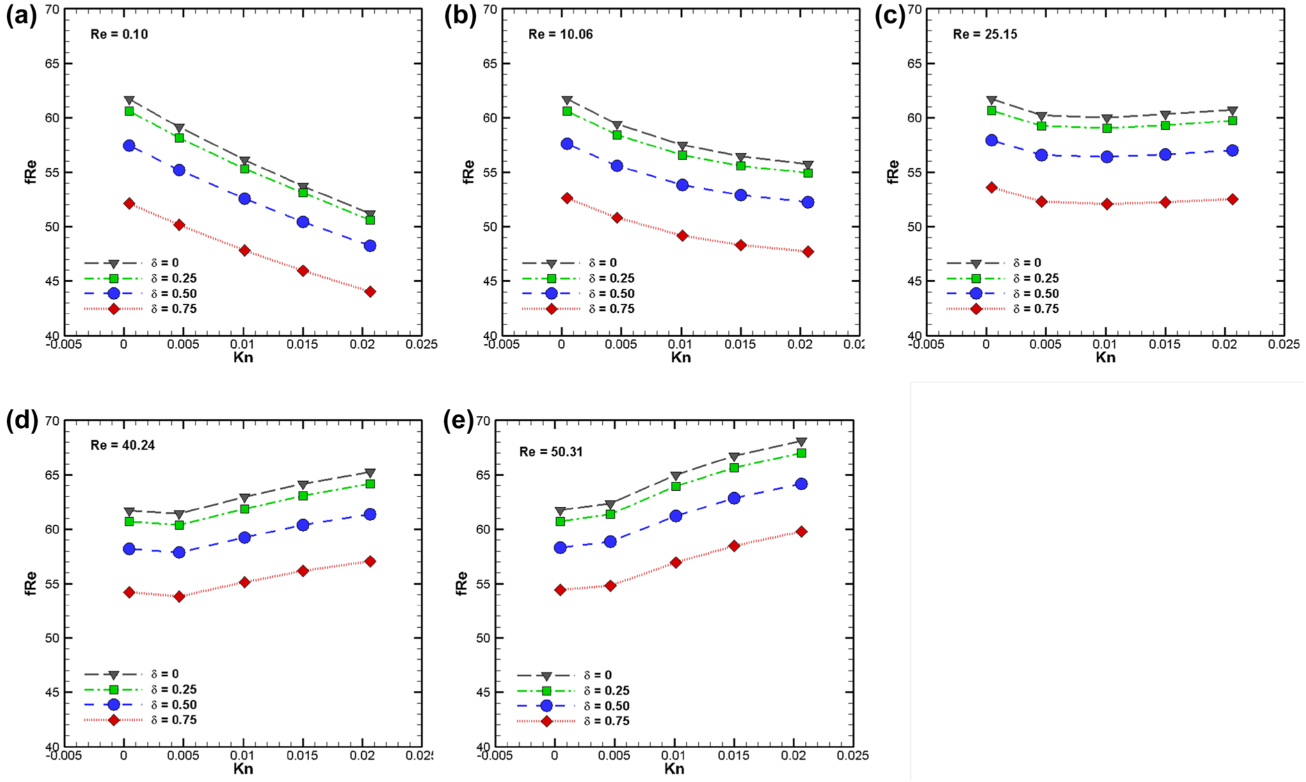

**Fig. 7** Effect of Knudsen number on Poiseuille number at various ridge fractions, compared to straight channel at Reynolds number **a** 0.10, **b** 10.06, **c** 25.15, **d** 40.24 and **e** 50.31

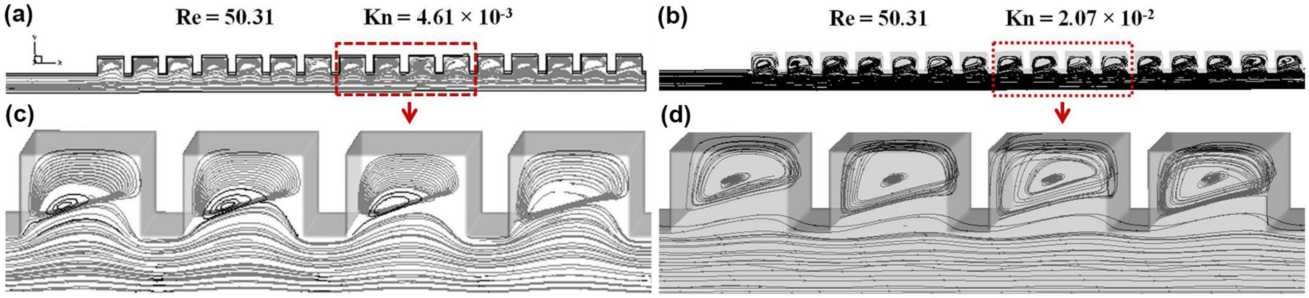

**Fig. 8** Comparison of streamtraces for 16 ridges of $\delta = 0.75$ at $Re = 50.31$; left column $Kn = 4.61 \times 10^{-3}$, right column $Kn = 2.07 \times 10^{-2}$. **a**, **b** entire 16 ridges; **c**, **d** magnified view of 8th, 9th, 10th and 11th ridges

### 3.4 Effect of TMAC on Poiseuille number

Tangential momentum accommodation coefficient (TMAC) is the fraction of tangential momentum lost when by a molecule on colliding a surface. For specular reflection, TMAC is zero signifying no accommodation, whereas for diffuse reflection, its value is 1, signifying total accommodation. In present work, TMAC is varied as 0.1, 0.3, 0.5, 0.7 and 0.926 as shown in Fig. 9. It is varied for across five different *Re* of this study at maximum exit *Kn* of $2.07 \times 10^{-2}$. In Eq. 9, inserting low values of TMAC increases the slip velocity, even for small values of *Kn* [2]. The more the value of TMAC, the more is the tangential momentum lost by a molecule on hitting the surface and less is the slip velocity. Hence, the gas molecules would slip less on the surface, leading to higher flow friction. This reflects the strong effect of slipping in reducing the Poiseuille number.

The dependence of Poiseuille number on TMAC is tremendously affected by modifying the surface topography using micro-ridges. In straight channel ($\delta = 0$), *fRe* is minimum at lowest value of TMAC = 0.1 for all

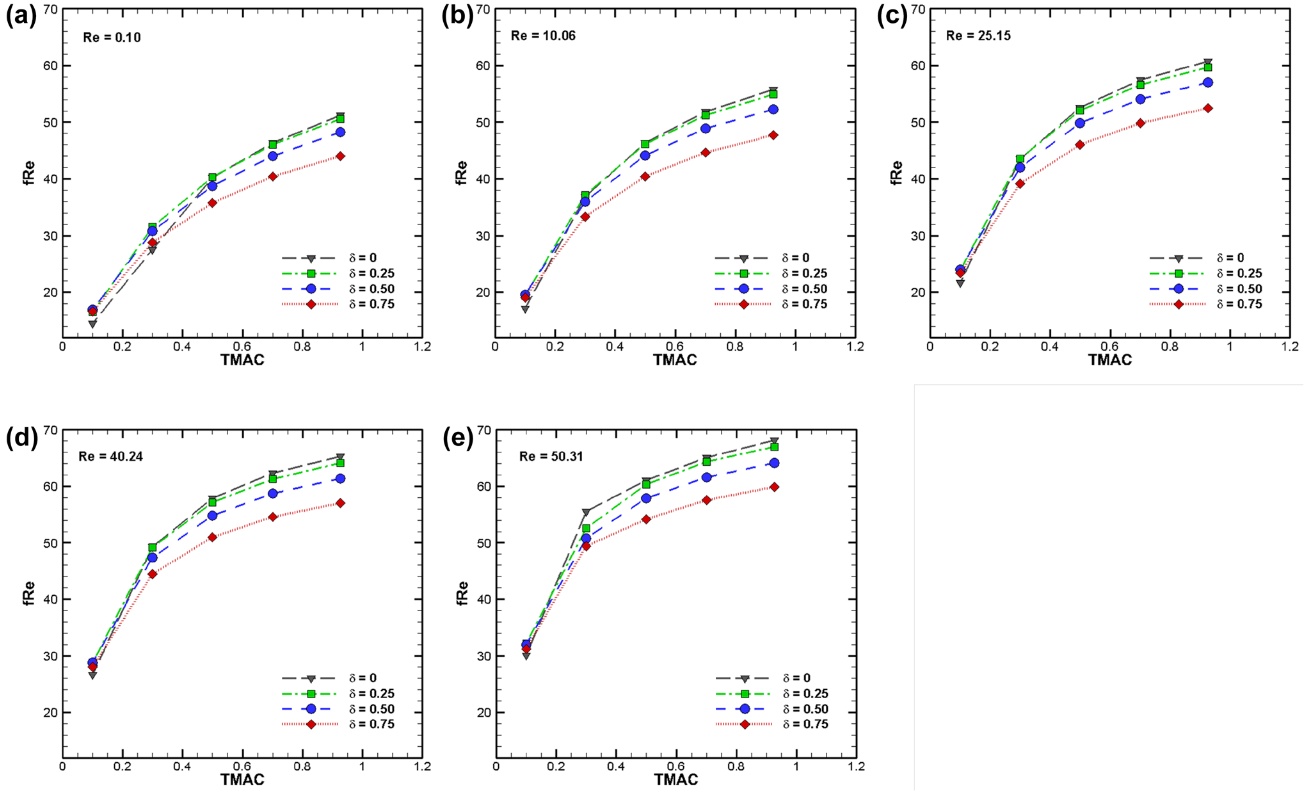

**Fig. 9** Effect of TMAC on Poiseuille number at various ridge fractions, compared to straight channel at Reynolds number **a** 0.10, **b** 10.06, **c** 25.15, **d** 40.24 and **e** 50.31

*Re* values. On contrary at highest TMAC = 0.926, *fRe* is maximum for $\delta = 0$. The role of ridges in reducing friction becomes effective after a threshold TMAC value. At lowest *Re* = 0.10, this threshold TMAC is less than 0.5, whereas at highest *Re* = 50.31, the threshold TMAC is less than 0.3. Hence, the threshold TMAC decreases with increase in Reynolds number. Below the threshold TMAC, there is high slipping already, which is enough for reduction of flow resistance. Introduction of ridges below this threshold TMAC is not helping at all in reducing the friction, since gas molecules are hardly able to appreciate the surface topography. After TMAC is more than a certain threshold, the loss of momentum of molecules increases and slipping decreases. This brings the need of changing the topography with ridges, which supports in drag reduction. The more is the ridge fraction, the less is the Poiseuille number. The results with shortest ridge length ($\delta = 0.25$) are almost overlapping with results with straight channel ($\delta = 0$). Longer ridge lengths ($\delta = 0.5$ and $\delta = 0.75$) are actually aiding in reduction of drag at high TMAC values. The reason is the increase in ridge length leading to increase in flow area, leading to less frictional resistance. Since, flow area is playing a major role in reducing friction, next we concentrate on changing the height of the ridge and studying its effect on *fRe.*

### 3.5 Effect of ridge height ratio on Poiseuille number

Ridge height ratio is the height of the ridge divided by half the height of channel (*h/H*). The height of the ridge is varied for each ridge fraction and influence of ridge height ratio on the Poiseuille number is studied in detail. Figures 10, 11, 12 and 13 signify that *fRe* decreases as the ridge height increases, up to a certain critical height ($h_c$), after which *fRe* becomes almost constant for a specific *Re* and *Kn*. Maximum *fRe* is observed in the case of lowest height. Beyond the ridge height of 100 µm (*h/H* = 1), there would not be any further considerable decrease in *fRe*. Hence, 100 µm height is chosen to explain the effect of *Re*, *Kn* and TMAC at all ridge fractions in the above sections and to calculate the critical height.

If a horizontal line is drawn at 1% increment of *fRe* obtained at *h/H* = 1, wherever it intersects *fRe* versus *h/H* curve, gives us the critical ridge height ratio ($h_c/H$). One should not take anything less than 1% because that would be within numerical uncertainty. The concept of critical height would be significant for designing low friction

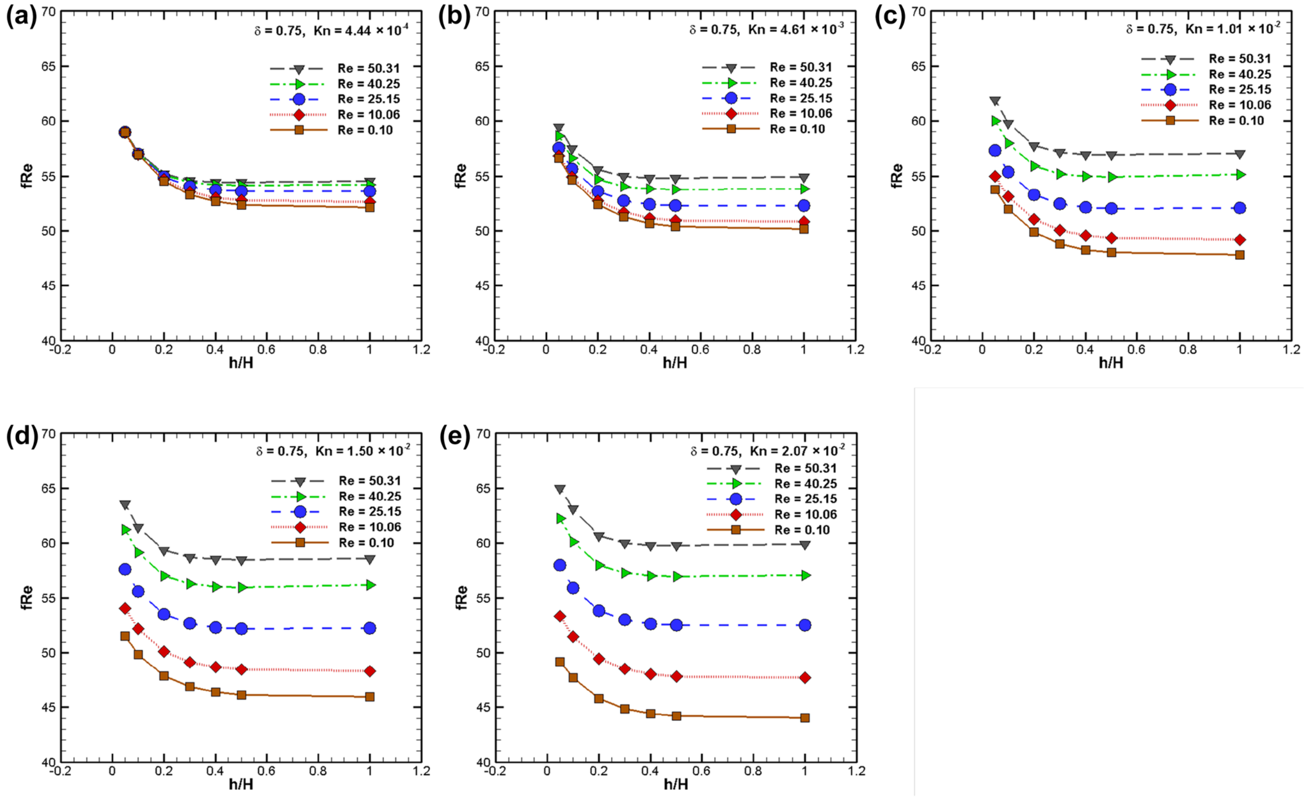

**Fig. 10** Effect of height of ridge on Poiseuille number at ridge fraction 0.75 at various exit Knudsen number **a** $4.44 \times 10^{-4}$, **b** $4.61 \times 10^{-3}$, **c** $1.01 \times 10^{-2}$, **d** $1.50 \times 10^{-2}$ and **e** $2.07 \times 10^{-2}$

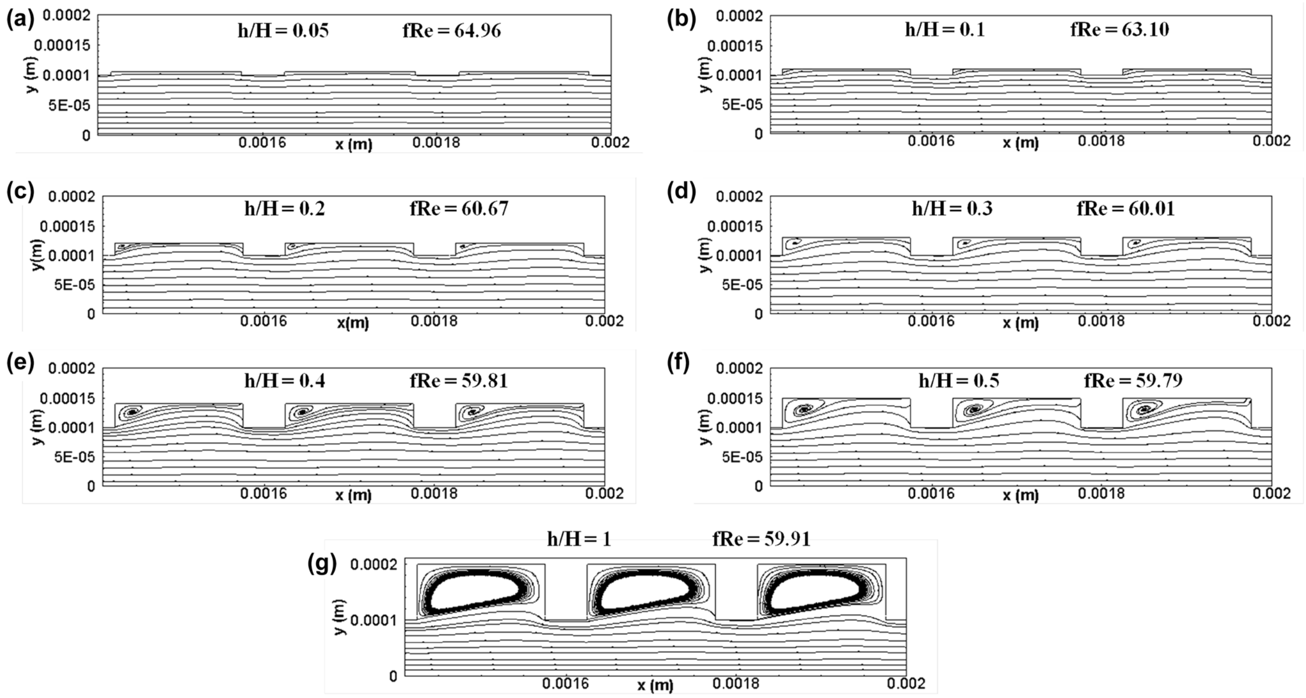

**Fig. 11** Streamlines at maximum exit $Kn = 2.07 \times 10^{-2}$ and maximum $Re = 50.31$ at different ridge heights of **a** 5 µm, **b** 10 µm, **c** 20 µm, **d** 30 µm, **e** 40 µm, **f** 50 µm and **g** 100 µm

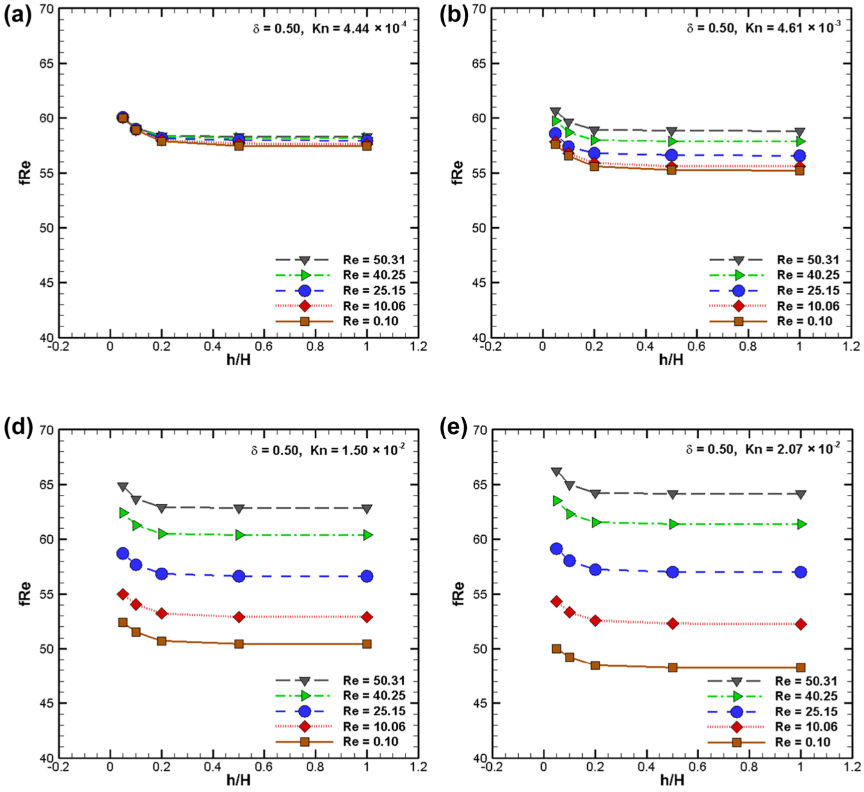

**Fig. 12** Effect of height of ridge on Poiseuille number at ridge fraction 0.50 at various exit Knudsen number **a** $4.44\times10^{-4}$, **b** $4.61\times10^{-3}$, **c** $1.01\times10^{-2}$, **d** $1.50\times10^{-2}$ and **e** $2.07\times10^{-2}$

channels. Ridge height chosen must be greater than the critical height for achieving low *fRe*. Therefore, greater is the value of critical height, more is the fabrication flexibility in choosing the ridge height without being concerned of increased flow friction. The detailed elucidation of critical height attained for each ridge fraction is provided in the following subsections.

### 3.5.1 Critical height for ridge fraction 0.75

The height of the ridge is varied as 5, 10, 20, 30, 40, 50 and 100 µm for $\delta=0.75$. As height increases up to 100 µm, *fRe* decreases up to height 50 µm, after which *fRe* is almost same at height 100 µm. In Fig. 10a, in the continuum regime, at heights of 5, 10 and 20 µm, there is no change in *fRe* with respect to *Re*. In Fig. 10b–e, as *Kn* increases, the effect of *Re* on *fRe* is prominent even at lower ridge heights. The range over which *fRe* varies with *Re* widens as the flow becomes more rarefied. *fRe* is inversely proportional to *Kn* and directly proportional to *Re*. After a certain ridge height ratio (h/H), there is no decrease in *fRe* at a specific *Re* value. Critical height ($h_c$) is found by intersection of a line drawn at 1% increment of *fRe* obtained at *h*/*H* = 1 with the *fRe* versus *h*/*H* curve. Such lines are drawn for all *Re* at a specific *Kn*. It is deduced from Fig. 10, at Re = 0.1, 30 µm < $h_c$ < 40 µm for all slip regimes. In continuum regime, lowest $Kn=4.44\times10^{-4}$, 40 µm < $h_c$ < 50 µm. At *Re* = 10.06, 30 µm < $h_c$ < 40 µm; whereas at *Re* = 25.25, 40.25 and 50.31, 20 µm < $h_c$ < 30 µm for all *Kn*. Therefore, ridge critical height reduces with increase in *Re*.

Figure 11 compares the streamline pattern for all the heights simulated for $\delta=0.75$ at $Kn=2.07\times10^{-2}$ and *Re* = 50.31. It is observed that vortex formation is absent for lower ridge heights of 5 and 10 µm. At 20 µm height, streamlines begin to curl at the left corner of the ridge, forming a counter-rotating vortex. The size of this vortex increases with increment in ridge height. Naris and Valougeorgis [16] too reported the growth of counterclockwise corner vortex on increasing the depth of a cavity in a compressible rarefied gas flow. Figure 11c, d depicts that left corner vortex size is the smallest for the range of critical height (20 µm < $h_c$ < 30 µm). Beyond $h_c$, the size of vortex increases upon incrementing the ridge height resulting in no significant reduction in *fRe*. The flow is asymmetric along the vertical centre-line of the ridge. According to Kuhlmann and Romanò [13], reflectional symmetry in *x*-direction is ruined at higher *Re*. Figure 3j depicts the *z*-vorticity to be lower at the right corner as

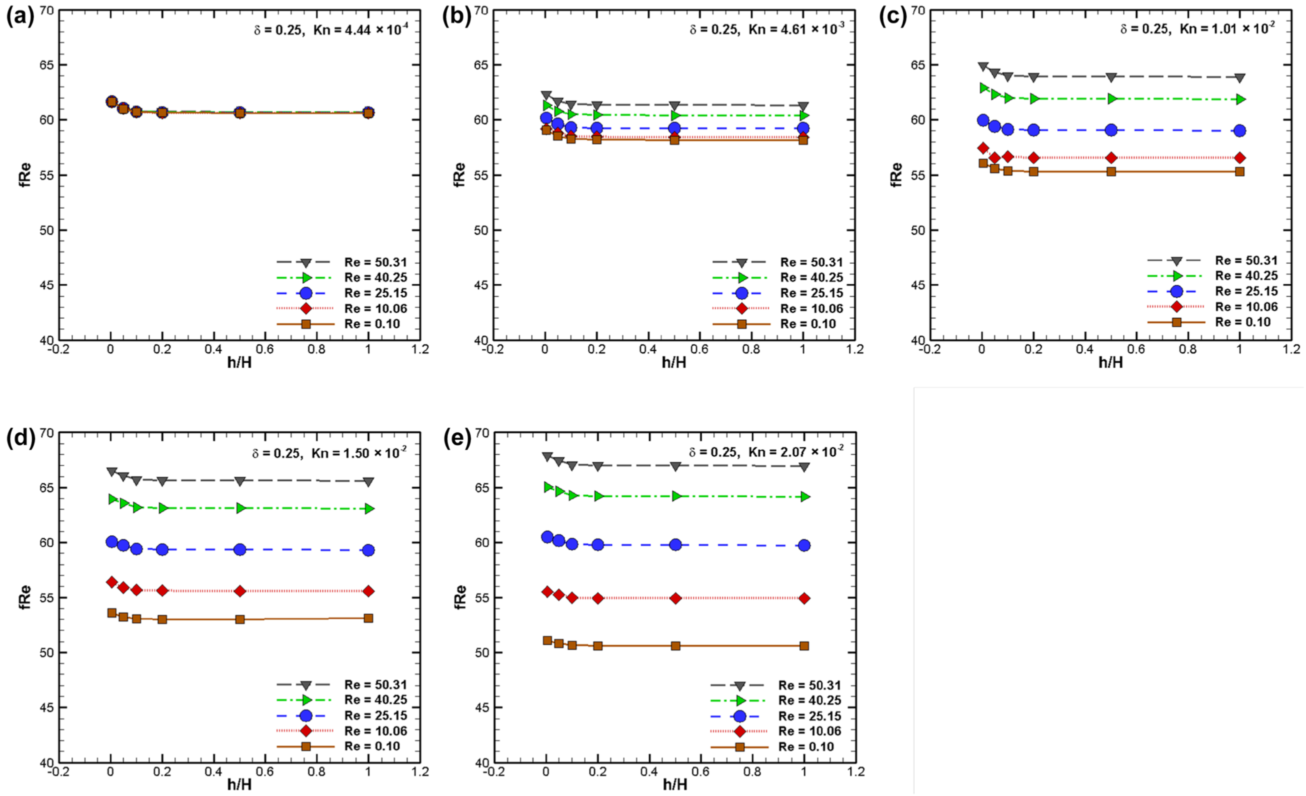

**Fig. 13** Effect of height of ridge on Poiseuille number at ridge fraction 0.25 at various exit Knudsen number **a** $4.44 \times 10^{-4}$, **b** $4.61 \times 10^{-3}$, **c** $1.01 \times 10^{-2}$, **d** $1.50 \times 10^{-2}$ and **e** $2.07 \times 10^{-2}$

compared to the left corner for the same flow conditions. This is because of the flow hitting the right corner before exiting the ridge. This creates higher pressure and lower velocity gradients at the right corner, leading to lower vorticity. This also explains the creation of vortex at left corner and not at the right corner in Fig. 11c–g. Interestingly, a trapped asymmetric vortex is created on further increasing the ridge height to 100 μm. This vortex hinders the penetration of streamlines into ridges and reduces the area available for flow expansion. In fact, there is a slight increment of 0.21% in *fRe* at 100 μm height with respect to *fRe* at 50 μm. This value might be within the numerical uncertainty, but at least there is no further decrement in *fRe*. This establishes the redundancy in further increasing the ridge height.

### 3.5.2 Critical height for ridge fraction 0.5

The height of the ridge is varied as 5, 10, 20, 50 and 100 μm for ridge fraction of 0.5 (Fig. 12). Since *fRe* obtained at 20, 50 and 100 μm heights are almost the same, there is no need of simulating heights 30 μm and 40 μm, unlike $\delta = 0.75$. Therefore, the effect of height at $\delta = 0.5$ is not as strong as seen in $\delta = 0.75$. In the continuum regime, at heights of 5 and 10 μm, there is no change in *fRe* with respect to *Re* (Fig. 12a). Similar to $\delta = 0.75$, *fRe* decreases with increasing *Kn* and increases with incrementing *Re* (Fig. 12b–e). There is no change in *fRe* as *h/H* increases beyond $h_c/H$. It is deduced from Fig. 12, for each *Kn* and *Re*, $10\ \mu\text{m} < h_c < 20\ \mu\text{m}$. The magnitudes of $h_c$ obtained for $\delta = 0.5$ is less than $h_c$ obtained at $\delta = 0.75$ at any specific *Re* and *Kn*.

### 3.5.3 Critical height for ridge fraction 0.25

For ridge fraction 0.25, the effect of height seen is the least (Fig. 13). The height of the ridge is varied as 0.5, 5, 10, 20, 50 and 100 μm for $\delta = 0.25$. Figure 13a indicates the overlapping of all *fRe* versus *h/H* curves indicating no effect of *Re* in the continuum regime. As *Re* decreases and *Kn* increases, *fRe* decreases. A slight decrease in *fRe* is observed till $h/H = 0.1$, beyond which *fRe* value is almost the same at any specific *Re* and *Kn*. It is deduced from Fig. 13, for each *Kn* and *Re*, $0.5\ \mu\text{m} < h_c < 5\ \mu\text{m}$. The magnitudes of $h_c$ obtained for $\delta = 0.25$ is less than $h_c$ obtained at $\delta = 0.5$ and $\delta = 0.75$ at any specific *Re* and *Kn*.

The range of $h_c$ has been provided in this study for all $\delta$, *Kn* and *Re*; its exact value could be found in future studies.

If the value of $h_c$ is higher, then there are more choices of ridge heights that could be fabricated without being concerned about an increase in flow friction. As the ridge fraction increases, ridge critical height increases at any specific *Re* and *Kn*. This indicates that the effect of increasing the ridge height for reducing the friction factor is most prominent in longest ridge length. The reason could be more area for the flow to expand, once it enters the ridge and then contract once it exits the ridge. The ability of the flow to penetrate into the ridge could be limited by the critical height. Beyond $h_c/H$, the streamlines might not be penetrating further, leading to a saturation of *fRe* value.

The above results certainly indicate that the presence of micro-ridges reduce the frictional resistance in rarefied gas flow.

## 4 Conclusions

The present three-dimensional numerical investigation of micro-scale gas flows through microchannel with ridges has led to the following conclusions:

1. Cuboidal micro-ridges play a significant role in reducing the frictional resistance in rarefied gas flows.
2. Poiseuille number reduces as the length and height of the ridge increases.
3. In all ridge fraction microchannels, *fRe* increases with *Re* in the slip flow regime.
4. *fRe* is inversely proportional to *Kn* at low *Re* and interestingly, *fRe* becomes directly proportional to *Kn* at high *Re* values.
5. *fRe* is directly proportional to the tangential momentum accommodation coefficient. The role of ridges in reducing the frictional resistance becomes effective at higher values of TMAC.
6. Critical height ($h_c$) of ridge is a major factor in deciding the ridge geometry which provides the least *fRe* value. The critical height is smallest for $\delta = 0.25$, followed by $\delta = 0.50$ and $\delta = 0.75$ at a specific *Re* and *Kn*.
7. $Re = 0.1$ and $Kn = 2.07 \times 10^{-2}$ provides the minimum *fRe* value of 44.02, obtained at $\delta = 0.75$ and $h/H = 1$. This is the lowest frictional resistance micro-ridge design recommended.

Present work sets no restriction in extending the height of ridge elements, since ridges protrude outward from the surface. Here, the height of highest ridge is of same order as the channel height and helps in drastic drag reduction. The existing literature on micro-cavities focuses more on shear driven [9–12] and lid-driven [13–16] liquid flows [24, 28] and not from the perspective of reducing friction in rarefied gas flows.

Our study concludes that ridges assist the upstream flow and decrease *fRe* due to increase in flow area for a specific *Re*, *Kn*, TMAC, $\delta$ and *h/H* range. The influence of threshold TMAC in reducing frictional resistance inside microchannels has been studied for the first time. The concept of choosing the ridge height greater than critical height would be significant for designing low friction channels. Contours of non-dimensional pressure, velocity, vorticity and streamtraces inside a micro-ridge are depicted to understand the dynamics of the flow. We recommend that care must be taken while selection of the ridge length and height for the working range of *Re*, *Kn* and TMAC. As a future work, the effect of ridges at higher *Kn* for a variety of shapes, orientations, number density and pitch can be studied.

**Acknowledgements** We sincerely thank Dr. Anvesh Gaddam, Dr. Majid Hassan Khan and Mr. Abhimanyu Gavasane, Department of Mechanical Engineering, IIT Bombay for technical discussions.

## Compliance with ethical standards

**Conflict of interest** The authors declare that they have no conflict of interest.

## References

1. Agrawal, A, Kushwaha H, Jadhav R (2019) Microscale flow and heat transfer: mathematical modelling and flow physics. Springer. https://doi.org/10.1007/978-3-030-10662-1
2. Mahulikar SP, Herwig H, Hausner O (2007) Study of gas microconvection for synthesis of rarefaction and nonrarefaction effects. J Microelectromech Syst 16(6):1543–1556. https://doi.org/10.1109/jmems.2007.908434
3. Darbandi M, Roohi E (2011) DSMC simulation of subsonic flow through nanochannels and micro/nano backward-facing steps. Int Commun Heat Mass Transf 38(10):1443–1448. https://doi.org/10.1016/j.icheatmasstransfer.2011.08.002
4. Croce G, D'Agaro P, Filippo A (2007) Compressibility and rarefaction effects on pressure drop in rough microchannels. Heat Transf Eng 28(8–9):688–695. https://doi.org/10.1080/01457630701326324
5. Khan HH, Sharma A, Srivastava A, Chaudhuri P (2015) Thermal-hydraulic characteristics and performance of 3D wavy channel based printed circuit heat exchanger. Appl Therm Eng 87:519–528. https://doi.org/10.1016/j.applthermaleng.2015.04.077
6. Sarkar M, Sharma A (2015) Fully-developed flow in a furrowed wavy channel: characterization of unsteady flow regimes and its effect on thermal-hydraulic performance. Numer Heat Transf A Appl 68(6):638–662. https://doi.org/10.1080/10407782.2014.994424
7. Harikrishnan S, Tiwari S (2018) Effect of skewness on flow and heat transfer characteristics of a wavy channel. Int J Heat Mass Transf 120:956–969. https://doi.org/10.1080/10407782.2014.994424
8. Shen C, Floryan JM (1985) Low Reynolds number flow over cavities. Phys Fluids 28(11):3191–3202. https://doi.org/10.1063/1.865366

9. Bres GA, Colonius T (2008) Three-dimensional instabilities in compressible flow over open cavities. J Fluid Mech 599:309–339. https://doi.org/10.1017/s0022112007009925
10. Horner M, Metcalfe G, Wiggins S, Ottino JM (2002) Transport enhancement mechanisms in open cavities. J Fluid Mech 452:199–229. https://doi.org/10.1017/s0022112001006917
11. De Vicente J, Basley J, Meseguer-Garrido F, Soria J, Theofilis V (2014) Three-dimensional instabilities over a rectangular open cavity: from linear stability analysis to experimentation. J Fluid Mech 748:189–220. https://doi.org/10.1017/jfm.2014.126
12. Romano F, Kuhlmann HC (2017) Particle–boundary interaction in a shear-driven cavity flow. Theoret Comput Fluid Dyn 31(4):427–445. https://doi.org/10.1007/s00162-017-0430-4
13. Kuhlmann HC, Romanò F (2019) The lid-driven cavity. In: Computational modelling of bifurcations and instabilities in fluid dynamics, Springer Cham, pp 233–309. https://doi.org/10.1007/978-3-319-91494-7_8
14. Shankar PN, Deshpande MD (2000) Fluid mechanics in the driven cavity. Annu Rev Fluid Mech 32(1):93–136. https://doi.org/10.1146/annurev.fluid.32.1.93
15. Mohammadzadeh A, Roohi E, Niazmand H (2013) A parallel DSMC investigation of monatomic/diatomic gas flows in a micro/nano cavity. Numer Heat Transf A Appl 63(4):305–325. https://doi.org/10.1080/10407782.2013.730463
16. Naris S, Valougeorgis D (2005) The driven cavity flow over the whole range of the Knudsen number. Phys Fluids 17(9):097106. https://doi.org/10.1063/1.2047549
17. Alkhalidi A, Kiwan S, Al-Kouz W, Alshare A (2016) Conjugate heat transfer in rarefied gas in enclosed cavities. Vacuum 130:137–145. https://doi.org/10.1016/j.vacuum.2016.05.013
18. Gat A, Frankel I, Weihs D (2008) Gas flows through constricted shallow micro-channels. J Fluid Mech 602:427–442. https://doi.org/10.1109/84.585795
19. Arkilic EB, Schmidt MA, Breuer KS (1997) Gaseous slip flow in long microchannels. J Microelectromech Syst 6(2):167–178. https://doi.org/10.1109/84.585795
20. Arkilic EB, Breuer KS, Schmidt MA (2001) Mass flow and tangential momentum accommodation in silicon micromachined channels. J Fluid Mech 437:29–43. https://doi.org/10.1017/s0022112001004128
21. Yu ZTF, Lee YK, Wong M, Zohar Y (2005) Fluid flows in microchannels with cavities. J Microelectromech Syst 14(6):1386–1398. https://doi.org/10.1109/jmems.2005.859086
22. Agrawal A, Prabhu SV (2008) Survey on measurement of tangential momentum accommodation coefficient. J Vacuum Sci Technol A Vacuum Surf Films 26(4):634–645. https://doi.org/10.1116/1.2943641
23. Dorari E, Saffar-Avval M, Mansoori Z (2015) Numerical simulation of gas flow and heat transfer in a rough microchannel using the lattice Boltzmann method. Phys Rev E 92(6):063034. https://doi.org/10.1103/physreve.92.063034
24. Gaddam A, Kattemalalawadi BS, Agrawal A, Joshi SS (2017) Demarcating wetting states in textured microchannels under flow conditions by Poiseuille number. Microfluid Nanofluid 21(8):137. https://doi.org/10.1007/s10404-017-1974-8
25. Gavasane A, Agrawal A, Pradeep AM, Bhandarkar U (2017) Simulation of a temperature drop for the flow of rarefied gases in microchannels. Numer Heat Transf A Appl 71(10):1066–1079. https://doi.org/10.1080/10407782.2017.1330091
26. Karniadakis, G., Beskok, A., & Aluru, N (2006) Microflows and nanoflows: fundamentals and simulation. Springer Science & Business Media (Vol. 29)
27. Morini GL, Spiga M, Tartarini P (2004) The rarefaction effect on the friction factor of gas flow in microchannels. Superlattices Microstruct 35(3–6):587–599. https://doi.org/10.1016/j.spmi.2003.09.013
28. Hemeda AA, Tafreshi HV (2016) Liquid–infused surfaces with trapped air (LISTA) for drag force reduction. Langmuir 32(12):2955–2962. https://doi.org/10.1021/acs.langmuir.5b04754